Pergamon

Acta mater. 48 (2000) 3773–3782

Acta MATERIALIA

www.elsevier.com/locate/actamat

# COMPUTER SIMULATION OF THE MICROSTRUCTURE AND RHEOLOGY OF SEMI-SOLID ALLOYS UNDER SHEAR

**M. PEREZ[1]*, J.-C. BARBÉ[2], Z. NEDA[3], Y. BRÉCHET[4] and L. SALVO[1]**

[1]Génie Physique et Mécanique des Matériaux, UMR CNRS 5010, BP 46, F-38402 Saint Martin d'Hères Cedex, France, [2]Laboratoire de Solidification et de ses Procédés, DTA/SPCM, CEA Grenoble, 17 rue des Martyrs, F-38054 Grenoble Cedex 9, France, [3]Babes-Bolyai University, Faculty of Physics, Department of Theoretical Physics, RO-3400 Cluj-Napoca, Romania, [4]Laboratoire de Thermodynamique et de Physico-Chimie Métallurgique, UMR CNRS 5614, BP 75, F-38402 Saint Martin d'Hères Cedex, France

*( Received 28 February 2000; received in revised form 15 May 2000; accepted 15 May 2000 )*

**Abstract**—The rheological behavior of metallic alloys containing both solid and liquid phases is investigated in the low solid fraction range (<50%). This behavior depends on both the solid fraction and the shear rate. The concept of effective volume fraction (EVF) is used to decorrelate the influence of these two parameters. At high shear rate the slurry behaves like a suspension of hard spheres, whereas at lower shear rate particles tend to aggregate in clusters, entrapping liquid and thus increasing the EVF and the viscosity. A lattice model is introduced to simulate the aggregation/break-up processes within a slurry under shear. When the steady state is reached, the entrapped liquid fraction is calculated, leading to a viscosity estimation. Simulation results for the viscosity and structure of the three-dimensional cluster are in good agreement with experimental results. 

*Keywords:* Casting; Semi-solid alloys; Theory & modeling

## 1. INTRODUCTION

Semi-solid slurries are characterized by the coexistence of solid and liquid phases. They are usually observed in alloys with two or more constituents for temperatures between the solidus and liquidus lines. The rheological properties of this dual-phase state is of interest both for casting and for metal forming operations known as thixoforming [1]. When submitted to shear, the steady-state viscosity decreases as the applied shear rate increases, reaching values of the order of 100 mPa s [2].

This behavior is called rheofluidization and it is usually explained by the interaction between the solid particles. It is a very general phenomenon observed in suspensions, metallic alloys in the semi-solid state, colloids, latexes, etc. Their characteristic behavior is qualitatively interpreted as a competition between the aggregating (Coulomb attraction, van der Waals' forces, surface forces, etc.) and break-up (shear) forces. At low shear rate (typically lower than 1 $s^{-1}$), individual particles can aggregate into "clusters" that are able to form a more or less rigid network and the slurry is considered as a solid. At very high shear rate, the motion of the particles prevents particle/particle bonding and leads to a more dispersed suspension behaving more like a fluid.

The concept of effective volume fraction (EVF) introduced by Quemada [3] allows one to relate the cluster characteristics to the viscosity of the mixture. The aim of the present paper is to build on this idea by considering the dynamics of cluster formation, and to derive a phenomenology for non-Newtonian behavior of a semi-solid slurry that is based on an understanding of the elementary phenomena governing the cluster dynamics.

Rheofluidization has been studied extensively (see the work of Quemada [4], for instance). Figure 1 shows a typical shear rate dependence of the viscosity for a suspension of interacting particles. Shear thickening, which may occur for higher values of the shear rate [5], is not considered. The behavior at high shear rate when particles are well separated has been accurately described by Krieger and Dougherty [6]:

$$\eta=\eta_0\left(1-\frac{\Phi}{\Phi_M}\right)^{-2.5\Phi_M}, \qquad (1)$$

$\Phi$ being the solid fraction of the suspension and $\Phi_M$ its maximum value (close packing). Below a given value $\dot{\gamma}_s$, an increase of the viscosity is observed. This can be interpreted as an increase in the effective volume fraction $\Phi_{eff}$, which takes into account both the

* To whom all correspondence should be addressed.

1359-6454/00/$20.00 
PII: S1359-6454(00)00161-0

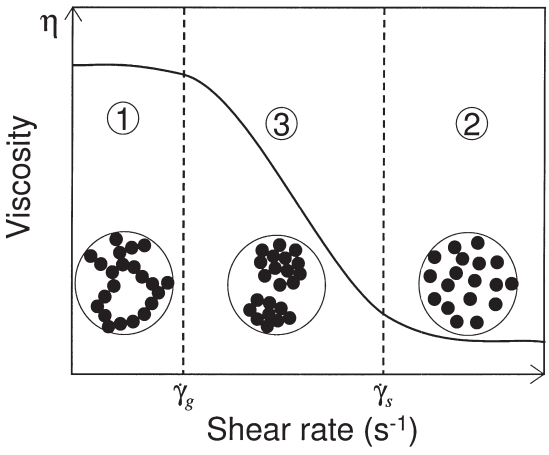


Fig. 1. Rheofluidization: viscosity decreases between the shear rates $\dot{\gamma}_g$ and $\dot{\gamma}_s$. 1—Percolating network, 2—dispersed suspension, 3—suspension of clusters.

solid and the entrapped liquid. $\Phi_{\text{eff}}$ replaces $\Phi$ in equation (1).

Jeffrey and Acrivos [7] underlined the notion of structure resulting from aggregation between solid particles: for the same solid fraction $\Phi$, different structures can lead to different viscosities. The structure itself depends on the shear rate. This statement is easily understandable for the two extreme limits of the shear rate: a "percolating network" for low shear rate and a "disperse suspension" for high shear rate. Between these two domains, the structure of diphasic solutions is not fully understood for several reasons:

- mean-field modeling fails to describe the dynamics of such slurries because it does not take into account the interaction between solid particles;
- two-dimensional (2D) observations are useful but not sufficient because they do not show the real state of aggregation. In particular, the three-dimensional (3D) connectivity of the solid particles cannot be easily revealed. Serial cutting [8] allows 3D reconstruction, but is only tractable for relatively small zones;
- the difficulty of 3D observations. Small-angle scattering is used efficiently [9] with colloids, but gives only a characteristic length scale of the suspension. Moreover, it is limited to small solid particles (less than a few micrometers). A new observational technique, synchrotron-radiation microtomography, is under development that should allow 3D investigation by means of phase contrast of a relatively large part of a sample with a resolution of a few micrometers [10].

In a previous work [11], an analytical estimation of the characteristic radius of clusters was derived by considering that aggregation and coalescence lead to spherical compact clusters. This radius was found to decrease with the shear rate as $\dot{\gamma}^{-4/7}$. In this paper we discuss the aggregation and break-up phenomena leading to more or less opened structures, neglecting the densification of the resulting clusters.

Different approaches have been used to simulate the rheological behavior of colloidal suspensions. Dynamic simulation tools such as non-equilibrium Brownian dynamics [12] and Stokesian dynamics [13] have provided insights into the influence of the various colloidal forces on the microstructure and the effect of this microstructure on suspension rheology. A non-dimensional structural parameter has been introduced to predict the rheology of aggregated sediment suspensions [14] and semi-solid slurries [15].

Based on simple physical assumptions, we propose in this paper an original computer simulation of the microstructure of a semi-solid metallic alloy submitted to shear. First, we discuss the parameters governing the structure, then we use a simple approach to relate the microstructure with rheological properties.

## 2. STRUCTURE AND VISCOSITY OF SHEARED SUSPENSION

The role of the solid fraction, $\Phi$, in the rheology of sheared suspensions has been studied extensively (e.g., see the review of Rutgers [16]). The law used most often for the $\Phi$ dependence of the viscosity is the Krieger phenomenological law. It has the advantage of pointing out the concept of maximum packing fraction, $\phi_{\text{M}}$.

The role of the shear rate is less clear. We know that it tends to break up the clusters, depending on the applied shear rate and the solid fraction. The possible structures can be grouped schematically into four different classes (see Fig. 2):

- at low solid fraction ($\Phi \leq \Phi_{\text{M}}$), the structure depends on the shear rate. At low shear rate (1), very little break-up occurs, leading to a 3D interconnected network. At high shear rate (2), the

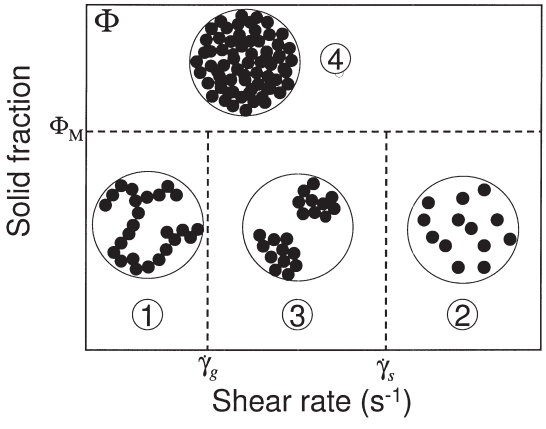


Fig. 2. Structure of the suspension in the ($\dot{\gamma}$,$\Phi$) phase-space. 1—Gel, 2—suspension of individual particles, 3—suspension of clusters, 4—compact arrangement. In this paper we are mostly interested in regions 2 and 3.

break-up process dominates leaving the system as a dispersed suspension (individual particles are well separated). In between these two domains (3), the aggregation and break-up processes counterbalance, leading to a suspension of clusters with $\dot{\gamma}$-dependent characteristic size and shape; and

- at high solid fraction ($\Phi \geq \Phi_M$), close packing is observed for any applied shear rate. The shear is then localized in particular planes.

The frontiers delimiting the different domains in Fig. 2 should be seen more as transition zones than strict boundaries.

In the dispersed suspension region the viscosity can be accurately described with a model developed for suspensions of hard spheres [see equation (1)]. In the 3D interconnected network region the deformation mechanisms are totally different, involving much more the solid than the liquid. Pseudo plastic models leading to a power law, $\eta = m\dot{\gamma}^{n-1}$, describe the rheology of the two-phase material successfully (see Ref. [17]).

In the intermediate region, Quemada [3] introduced the concept of EVF [$\Phi_{eff}$ in equation (2)] to replace the solid fraction $\Phi$ of equation (1), turning it into:

$$\eta = \eta_0 \left(1 - \frac{\Phi_{eff}}{\Phi_M}\right)^{-2.5\Phi_M}. \quad (2)$$

The EVF takes into account the entrapped liquid not involved in the hydrodynamic flow. $\Phi_{eff}$ is then the sum of the real solid fraction $\Phi$ and the part of the liquid that no longer takes part in the liquid flow. It could be, for example, the entrapped liquid in the middle of a solid aggregate. Note that liquid does not need to be completely surrounded by solid to be entrapped (see Section 4). On this basis, the structure of the suspension is re-injected into equation (1) through its correlation with the EVF. For a suspension of compact clusters, the EVF would be equal to the solid fraction, while for a more open structure (containing more entrapped liquid) it could be much higher than $\Phi$, leading to higher values of viscosity. The maximum packing fraction $\Phi_M$ characterizes a geometrical compactness. It is a function of the size and shape distribution of the individual solid particles and does not depend on $\dot{\gamma}$. The EVF takes into account the dependence of the microstructure as a function of the applied shear rate. The structure could have been introduced in a shear-dependent packing fraction $\Phi_M$ [18], instead of $\Phi$. Both approaches lead to the same results.

Ito *et al*. [8] used this concept to interpret experimental results on semi-solid slurries. After a time-consuming micrography analysis on many planes, they managed to give a 3D reconstruction of clusters resulting from stirring at steady state. They gave an estimation of the entrapped liquid fraction and plotted the measured viscosity versus EVF for slurries solidified under different shear rates. All of the experimental points were scaled back on a unique master curve.

The critical point of this analysis is the estimation of the structure-dependent EVF, as a function of the shear rate. In the following section, we propose an approach to predict the structure evolution of a semi-solid slurry submitted to shear.

## 3. THE STEADY STATE OF SHEARED SUSPENSION: COMPETITION BETWEEN AGGREGATION AND BREAK-UP

When a semi-solid slurry is left at rest, two different mechanisms occur:

- Oswald ripening [19] and spheroidization tend to minimize the solid/liquid surface energy by narrowing the size distribution of the aggregates and smoothing the surfaces of the solid particles. These phenomena are diffusion-limited with a characteristic length of the order of the individual particle radius, $a_0$. A characteristic diffusion time could be approximated by: $a_0^2/D \approx 2$ s, where $D \approx 5\times10^{-9}$ m$^2$s$^{-1}$ is the diffusion coefficient of the solute in the liquid and $a_0 \approx 100$ μm; and
- particle aggregation occurs to lower the liquid/solid surface energy. The driving force of aggregation is the difference between twice the solid/liquid surface energy and the solid/solid surface energy: $\Delta\sigma = 2\sigma_{SL} - \sigma_b$. The aggregation kinetics is limited by the collision frequency, which is estimated in [20] for a sheared suspension of hard spheres as $f_c = (8/\pi)\Phi\dot{\gamma}$. In the intermediate region of Fig. 2, the characteristic time between two collisions ($1/f_c$) ranges from 1 s to 1 ms when $\dot{\gamma}$ ranges from 10 to 1000 s$^{-1}$.

In the present paper, we are interested in a shear rate domain where the kinetics of aggregation is much more rapid than the kinetics of Oswald ripening (see above). We will then neglect Oswald ripening. Indeed, in a relevant time for diffusion-limited mechanisms, aggregation induces more drastic changes in the microstructure than Oswald ripening.

The aggregation mechanism is collision-induced. We are interested in the physical mechanisms taking place during the contact between two particles. Two spherical objects of radius $a_0$ aiming at one another in a shear flow with shear rate $\dot{\gamma}$ will meet during a mean contact time $\tau_c$ approximated by Adler *et al*. [21] for the limit of small solid fraction as:

$$\tau_c = \frac{5}{2}\dot{\gamma}^{-1}. \quad (3)$$

During the contact, if a favorable crystallographic orientation is encountered, a rigid neck will be built

between the two particles (see Fig. 3). We now use a result derived in Ref. [15] concerning the growth rate of a neck between two solid spherical particles of radius $a_0$ (see Fig. 3). If $x$ is the neck radius and $\tau_f$ the neck formation time after collision of the particles, $\tau_f$ follows:

$$\tau_f = \frac{1}{5} A\left(\frac{x}{a_0}\right)^5 a_0^3, \tag{4}$$

where A is a constant dependent on thermophysical properties of the material (see Ref. [11] for more details). Assuming that the neck builds up during the contact time $\tau_c$, we have $\tau_c=\tau_f$, leading to an estimation of the neck size:

$$x=\left(\frac{25}{2A}\right)^{1/5} \dot{\gamma}^{-1/5} a_0^{2/5}. \tag{5}$$

The shear will tend to break the aggregates during collision. As collision of two clusters of size $\Delta L$ occurs their mean relative velocity is $(\Delta L/2)\dot{\gamma}$. Thus, the kinetic energy $E_c$ available for rupture is:

$$E_c = \frac{1}{2} \rho V\left(\dot{\gamma}\frac{\Delta L}{2}\right)^2, \tag{6}$$

where $\rho$, $V$, $\dot{\gamma}$ and $\Delta L$ are the mass density, the volume, the shear rate and the size of the cluster in the normal direction of the rupture plane, respectively. $E_c$ has to be compared with the energetic cost of the plastic rupture (classically considered to be 1000 times larger than the fragile rupture energy [22]):

$$Er=n\pi x^2 1000\Delta\sigma, \tag{7}$$

$n$ and $\Delta\sigma$ being the number of broken necks of size $x$ [defined in equation (5)] in the fracture plane and the energy cost due to liquid/solid surface creation, respectively.

If $\dot{\gamma}$ is small, the contact time $\tau_c$ is long and necks will be large. Moreover, the kinetic energy will be low, preventing any break-up of the resulting cluster. This situation will lead to the formation of a rigid 3D network. For large $\dot{\gamma}$ the contact time is short and the kinetic energy is large enough to prevent any aggregation. This leads to a dispersed suspension. As both aggregation and break-up are collision-induced, the collision frequency influences only the kinetics of aggregation/break-up but does not influence the equilibrium between these two mechanisms.

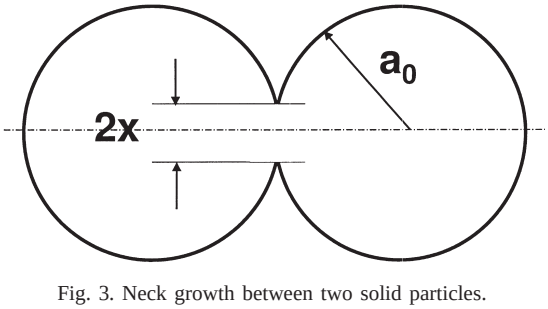


Fig. 3. Neck growth between two solid particles.

In the present study, we deal with "liquid-driven deformation". This means that the shear rate is sufficiently high to allow the competition between aggregation and break-up, the deformation being allowed by the free liquid between the clusters.

From these simple considerations, the probabilities of aggregation and break-up between particles and clusters of particles will be derived and used to simulate cluster dynamics.

## 4. LATTICE MODEL SIMULATION OF CLUSTER STRUCTURE

In a real system containing $\approx 10^5$ particles, one would have to treat $\approx 10^3$ clusters in order to be representative of the distribution. This is untractable with standard computer power. We are interested here in steady-state interaction, which means a dynamical equilibrium between cluster aggregation and cluster fracture. We assume a sort of "ergodic" hypothesis, namely that in steady state, the size distribution of a population of clusters at a given time is equivalent to the size distribution of a given cluster along time. Our main simplifying approach based on the above hypothesis is in considering only one representative cluster that can either aggregate with its copy, or can be broken in a random plane. The time evolution of this cluster will approximate the ensemble properties of the equilibrium semi-solid slurry.

The cluster is made up of a cubic arrangement of connected spheres (elementary particles of radius $a_0$). It is stored in a 3D matrix (cubic lattice), where 0 stands for free liquid, 1 stands for solid and 2 stands for entrapped liquid. The size of the matrix unit cell ($2a_0$) is chosen so that the elementary particle is inscribed into this cubic unit cell.

### *4.1. Aggregation*

The aggregation probability $P_a$ per collision is assumed to be the probability $q_e$ for two particles to encounter with a favorable crystallographic orientation. As in Ref. [15], we consider that only a low-angle grain boundary ($\leq$0.25 rad) will give rise to a non-wetted grain boundary, leading to $q_e$=0.02. This condition is equivalent to:

$$P_a = q_e. \tag{8}$$

### *4.2. Break-up*

The rupture probability per collision $P_r$ should be a monotonically increasing function of the ratio of the available kinetic energy over the energetic cost of the rupture ($E_c/E_r$). At zero kinetic energy it should be zero, and for $E_c=E_r$ it should converge to 1. The most simple form satisfying the above criterion is the simple $P_r=E_c/E_r$ approximation. A fracture plane is ran-

domly chosen. The differential kinetic energy introduced in [11] is given by equation (6). The volume $V$ of the cluster is taken as $(e+s)(2a_0)^3$, with $e$ and $s$ being the number of entrapped liquid voxels and the number of solid particles in the cluster, respectively. The energetic cost of the rupture is given by equation (7). We then have the rupture probability per collision:

$$P_r = \frac{E_c}{E_r} = \frac{2\ \rho a_0^{21/5}}{125\,\pi\Delta\sigma}\left(\frac{25}{2A}\right)^{-2/5} \times \frac{(e+s)(\Delta L/4a_0)^2\dot{\gamma}^{12/5}}{n}. \tag{9}$$

The first group of terms in equation (9) depends on material properties ($\rho$, $\Delta\sigma$, A) and the initial state ($a_0$), whereas the second member is calculated at each step of the simulation.

During cluster/cluster collisions, aggregation or rupture may occur. However, most of the time, neither aggregation nor break-up occurs and the two clusters are left as before. As we deal with the steady state there is no need to consider these collisions with no effect. The only parameter is then the ratio $P_a/P_r$:

$$\frac{P_a}{P_r} = K\frac{n}{(e+s)(\Delta L/4a_0)^2\dot{\gamma}^{12/5}}, K = \frac{125\pi q_e\Delta\sigma}{2\ \rho a_0^{21/5}}\left(\frac{25}{2A}\right)^{2/5}. \tag{10}$$

Through equation (10), K incorporates the material properties and the initial state. For an Al–6.5 wt% Si alloy with a 50 μm globular structure, $K=5\times10^8\ s^{-12/5}$ (see Table 1).

For each step, the one-cluster algorithm randomly selects a rupture plane and calculates the break-up probability (aggregation probability is fixed to $q_e$). A number is randomly generated between 0 and $P_a+P_r$:

- if it ranges between 0 and $P_r$, fracture is processed by deleting all solid particles belonging to the rupture plane. One of the resulting clusters is randomly selected and stored in the matrix M; or else
- the cluster is duplicated in a matrix N, randomly rotated, and the two matrices, M and N, are then aggregated allowing interpenetration. The resulting cluster is stored in the matrix M.

Aggregation and rupture mechanisms are illustrated in Fig. 4 and a simplified algorithm of the numerical simulation is shown in Fig. 5.

The number of solid particles $s$, the number of entrapped liquid voxels $e$ and the gyration radius $R$ are extracted from the matrix M, leading to the calculation of the effective volume fraction. The gyration radius is defined as the mean distance between the cluster center of mass and all of its solid particles. Averages ($\bar{R}$, $\bar{s}$, $\bar{e}$) are calculated over the total step number. Since the mean "lifetime" between two collisions is assumed to be independent of the cluster radius, there is no need to weight the averages.

Table 1. Symbols, their meanings and values for Al–6.5 wt% Si

| Symbol | Meaning |
|---|---|
| A | Constant depending on thermophysical parameters ($1.7\times10^{16}$ s m$^{-3}$) [11] |
| $a_0$ | Initial particle radius |
| D | Diffusion coefficient of the solute in the liquid ($5\times10^{-9}$ m$^2$ s$^{-1}$) |
| $d_1$, $d_2$, $d_3$ | Distance between a liquid voxel and the nearest solid particle in the directions (**Ox**), (**Oy**), (**Oz**) |
| $E_b$ | Rupture energy of a cluster |
| $E_c$ | Kinetic energy of a cluster |
| $e$, $\bar{e}$ | Number and mean number of entrapped liquid voxels in a cluster |
| $f_c$ | Collision frequency of clusters in a shear field |
| K | Physical constant defined in equation (10) |
| $\Delta L$ | Size of the cluster in the normal direction of the rupture plane |
| M, N | 3D matrices used to store the cluster |
| $n$ | Number of necks in the fracture plane |
| $P_a$ | Aggregation probability |
| $P_r$ | Breaking probability |
| $q_e$ | Probability for two particles to encounter with favorable crystallographic orientation |
| $R$, $\bar{R}$ | Cluster gyration radius and cluster mean gyration radius |
| $s$, $\bar{s}$ | Number and mean number of solid particles in a cluster |
| $V$ | Volume of the cluster (solid+entrapped liquid) |
| $x$ | Neck radius |
| $\dot{\gamma}$ | Shear rate |
| $\dot{\gamma}_g$ | Gelation shear rate |
| $\dot{\gamma}_s$ | Shear rate from which no aggregation occurs |
| $\eta$ | Viscosity of the suspension |
| $\eta_0$ | Viscosity of the liquid (20 mPa s) [8] |
| $\rho$ | Density (2350 kg m$^{-3}$) |
| $\sigma_b$ | Grain boundary surface energy (negligible; Coincidence Site Lattice hypothesis) |
| $\sigma_{SL}$ | Liquid/solid surface energy (0.17 J m$^{-2}$) |
| $\Delta\sigma$ | Surface energy due to liquid/solid surface creation (0.34 J m$^{-2}$) |
| $\tau_c$ | Contact time between two particles in a shear field |
| $\tau_f$ | Formation time of a neck between two particles |
| $\Phi$ | Volumic solid fraction |
| $\Phi_{eff}$ | Effective volume fraction (EVF) |
| $\Phi_M$ | Maximum packing fraction |

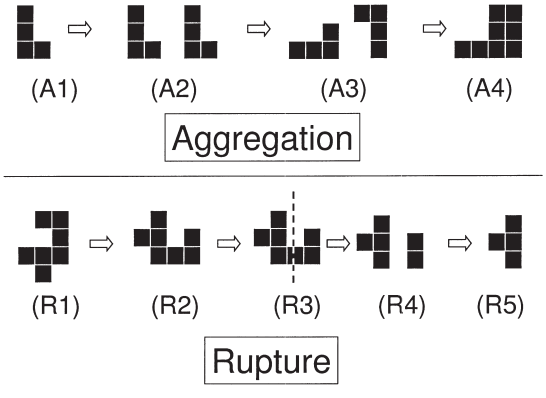


Fig. 4. Aggregation process: (A1) initial cluster→(A2) initial cluster is duplicated→(A3) random rotation→(A4) sticking of the two clusters. Rupture process: (R1) initial cluster→(R2) random rotation→(R3) random selection of a fracture plane→(R4) erasing the particles in the fracture plane→(R5) random selection of the resulting cluster. Note that the fracture probability depends on the number of necks to be broken in the fracture plane.

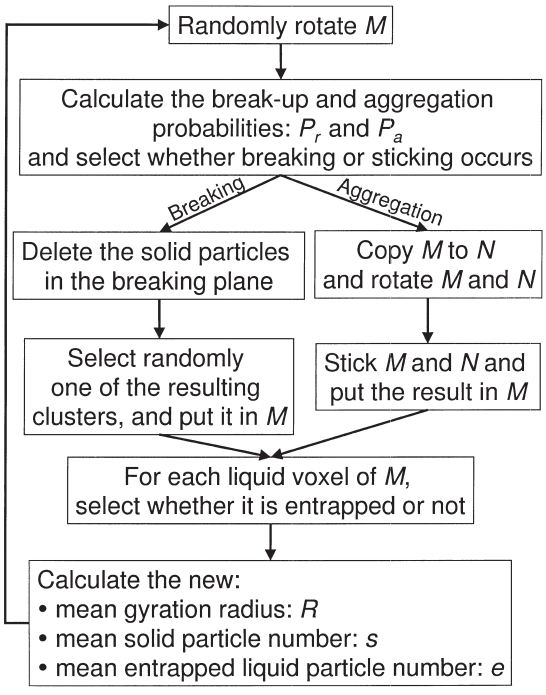


Fig. 5. Simulation algorithm: the cluster is stored in $M$ and $N$ (3D matrices).

One of the crucial points of this simulation is the evaluation of the entrapped liquid in the cluster. Indeed, this effect governs the effective volume fraction $\Phi_{\text{eff}}$ that will be introduced in equation (2) to predict the viscosity. It is calculated at each step and defined as follows: a liquid voxel is entrapped if four or more of its six principal directions (cubic lattice) (**Ox**, **Ox**, **Oy**, **-Oy**, **Oz**, **-Oz**) hit any solid particle of the cluster. If only three directions out of the six point to a solid particle, the liquid is entrapped if the averaged distance between the considered liquid voxel and the three intersected solid particles is smaller than the cluster gyration radius $R$. In other terms, if $d_1$, $d_2$ and $d_3$ are the distances between the liquid voxel and the nearest solid particle in the three directions considered, the liquid is entrapped if $d^2{}_1+d^2{}_2+d^2{}_3<R^2$. For a better understanding, this procedure is visualized in Fig. 6 for the 2D case.

## 5. NUMERICAL VALIDATION

The simulation starts with a cluster constituted of one solid particle. It usually grows until it reaches a large enough size to be broken. A typical time evolution of the cluster gyration radius $R$ is shown in Fig. 7 for a shear rate of 500 $s^{-1}$. Although the gyration radius $R$ fluctuates strongly in time, the distribution of $R$ is stable. The numerical convergence is reached when fluctuations of the distribution are less than 10%. Fig. 8 displays the cluster gyration radius distribution after various computation steps. Steady state is reached after $\approx$5000 steps.

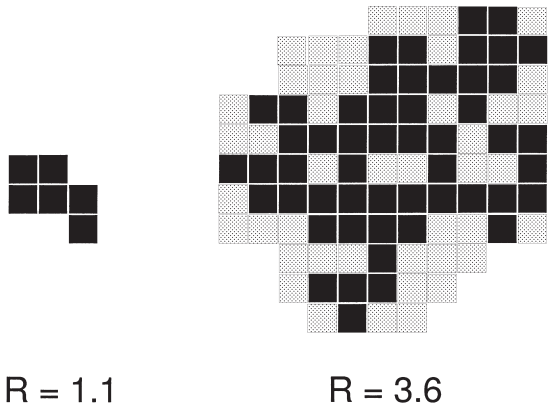


Fig. 6. Representation of the entrapped liquid (gray) for a 2D cluster: the liquid is entrapped if three or four of the principal directions point to any solid particle (black). In the case of two directions pointing to solid particles, the mean distance to the solid is compared with the cluster gyration radius.

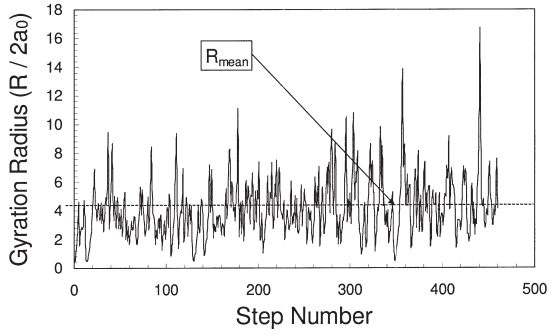


Fig. 7. Time evolution of the cluster gyration radius. $R$ fluctuates a lot, but its time evolution is assumed to be representative of the spatial distribution of the clusters.

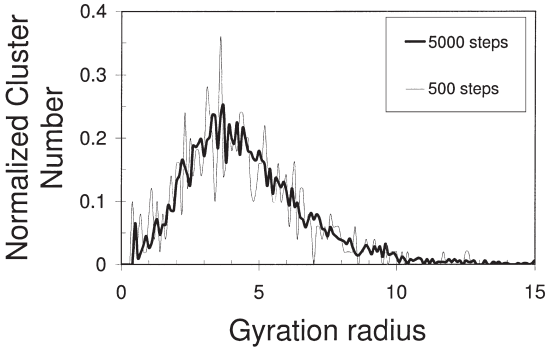


Fig. 8. Distribution of $R$ after various computation steps. Steady state is reached when distribution fluctuations are less than 10%.

## 6. RESULTS

The results of the simulation will be presented as follows:

1. the 3D cluster shape at different shear rates will be depicted;

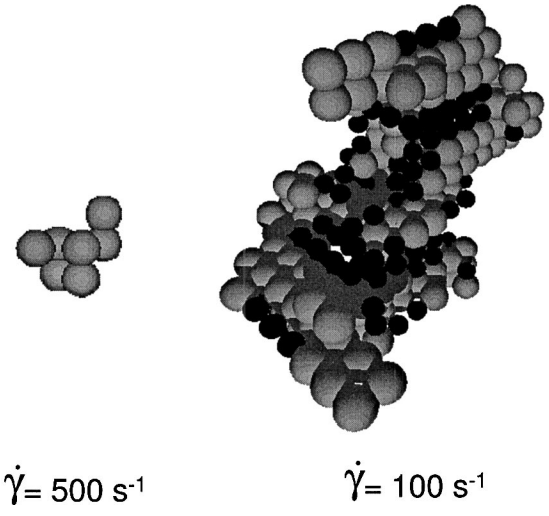


Fig. 9. Clusters for two different shear rates. Liquid is transparent, solid is gray, and entrapped liquid is black. A larger cluster corresponds clearly to a higher entrapped liquid fraction.

2. the size distribution of clusters for different shear rates will be plotted and compared with an analytical model available in the literature;
3. the $\dot{\gamma}$ dependence of the mean radius $\bar{R}$ of the clusters will be discussed;
4. the parameter $\Phi_{\text{eff}}/\Phi$ will be computed as a function of the shear rate, giving a more precise structure map than the one given in Fig. 2; and
5. finally, the viscosity $\eta$ will be given as a function of the shear rate and the solid fraction.

### 6.1. Cluster shape

Fig. 9 shows a cluster of radius $R$ with its entrapped liquid for two different shear rates. For small $\dot{\gamma}$ aggregation is dominant, leading to a more open structure entrapping more liquid.

### 6.2. Cluster size distribution

Fig. 10 exhibits normalized radius distributions for different shear rates. The size distribution of particles can be accurately described by a "log-normal" law, frequently encountered in fragmentation problems (see Ref. [23]). Since these experiments are ensemble distributions, whereas our simulation deals with time evolution, this similarity gives some confidence to the "ergodic"-type hypothesis used herein.

The normalization brings the simulated distribution for various shear rates to a single master curve. The size dispersion is then proportional to the mean size of the clusters: the lower the shear rate, the larger the mean cluster radius and the larger the size dispersion. For low shear rate, the cluster can explore either small and large sizes, whereas for high shear rate, only small sizes are possible.

In Fig. 10, one can compare the simulated distribution with the mathematical model of Takajo *et al.* [24] often used as a model for aggregation processes. This model, based on homogeneous coalescence frequency, gives a normalized size distribution at steady state. These two different approaches lead to comparable profiles, giving some confidence into the general basis of our simulation.

### 6.3. Mean cluster radius versus shear rate

The mean gyration radius values obtained are plotted as a function of the shear rate in Fig. 11. The mean gyration radius $\bar{R}$ decreases with increasing shear rate following a power law, $\bar{R} \propto \dot{\gamma}^{-0.7}$. This dependence is comparable with the power law estimated for the compact cluster scenario [11]: $R \propto \dot{\gamma}^{-0.6}$. It can be observed that, above a given $\dot{\gamma}$, only elementary particles remain and hence there is no further evolution of $\bar{R}$.

As the physical parameter K depends strongly on the size of the individual particles $a_0$ [see equation (10)], computations are presented for two different reasonable values of $a_0$. For the smaller elementary particle size, the clusters are larger at some given shear rate and solid fraction.

### 6.4. Effective volume fraction versus shear rate

Fig. 12 displays the calculated ratio $\Phi_{\text{eff}}/\Phi$ as a function of $\dot{\gamma}$ for two different elementary particle sizes. For high $\dot{\gamma}$ (high enough to break all of the

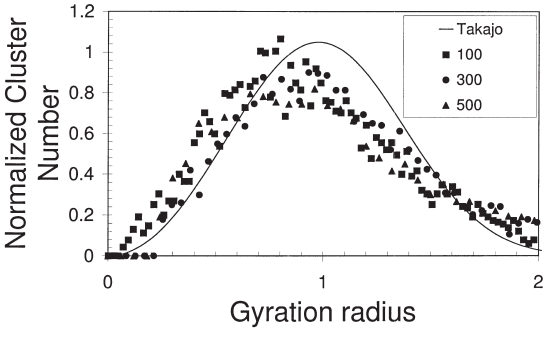


Fig. 10. Gyration radius distribution for 5000 simulation steps at various shear rates compared with the mathematical model of Takajo *et al.* [24].

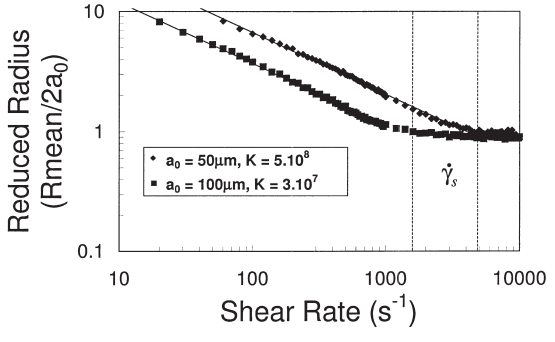


Fig. 11. The $\dot{\gamma}$ dependence of the mean gyration radius. For $\dot{\gamma}$ higher than $\dot{\gamma}_s$, the shear breaks the clusters into individual particles.

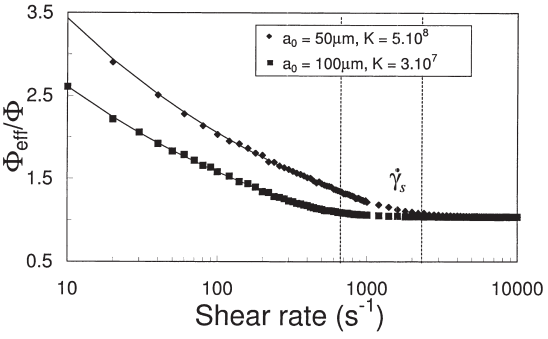


Fig. 12. The ratio $\Phi_{eff}/\Phi$ as a function of $\dot{\gamma}$ for two values of the simulation constant corresponding to two initial particle sizes. For $\dot{\gamma}$ higher than $\dot{\gamma}_s$, the structure is too small to trap any liquid.

necks), there is no entrapped liquid ($\Phi_{eff}/\Phi$=1). For small $\dot{\gamma}$, more connected structures lead to a high fraction of entrapped liquid ($\Phi_{eff}/\Phi \approx 2$).

In Fig. 13 we can identify the three different domains introduced in Section 2 (Fig. 2).

- For high $\dot{\gamma}$ values ($\geq \dot{\gamma}_s$), the dispersed suspension-like behavior is observed. $\dot{\gamma}_s$ is reached when the mean radius of the clusters is equal to the radius of the elementary solid particles, that is to say when the effective volume fraction is equal to $\Phi$. Note that an approximation of $\dot{\gamma}_s$ can be obtained by making $P_a$ and $P_r$ equal in equation (10). We find for Al–6.5 wt% Si with initial particle size $a_0$=100 μm: $\dot{\gamma}_s$=1300 s$^{-1}$. This value is clearly in accordance with the transition domain of Fig. 12.
- For low $\dot{\gamma}$ values ($\geq \dot{\gamma}_n$) a rigid network sets in. The estimation of $\dot{\gamma}_n$ depends on the gelation mechanism:
  - experimentally, the apparent rigid network will appear when the mean radius of the clusters reaches the characteristic size of the measurement apparatus (Couette rheometer, for example);
  - in theory, the apparent rigid network will appear when EVF=$\Phi_M$: the whole volume of the sample is invaded by a unique cluster.$\dot{\gamma}_n$ is found to be $\Phi$-dependent. We can observe that the simulation leads to a more realistic description of the structure (Fig. 13) than in Fig. 2. Indeed, the lower the solid fraction, the higher the liquid fraction involved in the hydrodynamic flow for some given $\dot{\gamma}$ and aggregation state characterized by *e* and *s*.
- In the intermediate range we have a suspension of clusters with decreasing size and entrapped liquid fraction as $\dot{\gamma}$ increases.

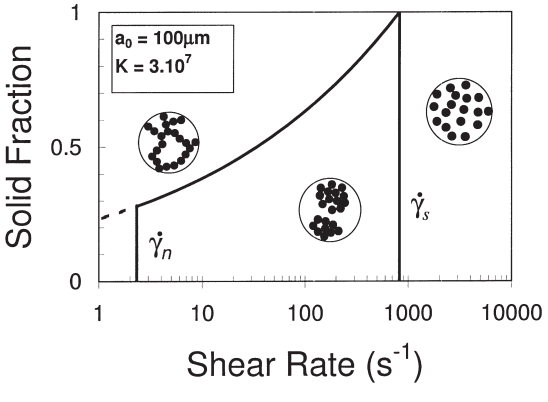


Fig. 13. Suspension structure depending on $\dot{\gamma}$ and $\Phi$. $\dot{\gamma}_n$ is now $\Phi$-dependent, except at low solid fraction where gelation occurs when a cluster reaches the size of the apparatus gap (left vertical line).

### 6.5. *Viscosity versus shear rate*

For the calculation of the viscosity, the entrapped liquid is taken into account through (a) the mean number of entrapped liquid voxels $\bar{e}$, and (b) the amount of entrapped liquid within a cubic voxel containing a solid sphere, which depends on the mean number $n_n$ of solid neighbors of a particle over the 26 possible neighbors in the cubic lattice. The liquid fraction within a unit cell is 0.42 (difference between the volume of the cube and that of its inscribed sphere). The viscosity follows:

$$\eta=\eta_0\left(1-\frac{\Phi_{eff}}{\Phi_M}\right)^{-2.5\Phi_M}, \qquad (11)$$

$$\Phi_{eff}=\Phi\left(1+\frac{\bar{e}}{\bar{s}}+\frac{0.42(n n/26)}{s}\right),$$

where $\bar{e}$ and $\bar{s}$ are the mean number of entrapped liquid sites and the mean number of solid sites in the cluster, respectively. With a suspension of hard spheres, $\Phi_M$ would have been 0.65, but as we deal with polydisperse and deformable solid particles, it is chosen to be 1. Indeed, the liquid phase has been proved to remain connected for solid fraction up to 0.8.

These equations lead to Fig. 14, where viscosity is plotted versus the solid fraction. The viscosity exhib-

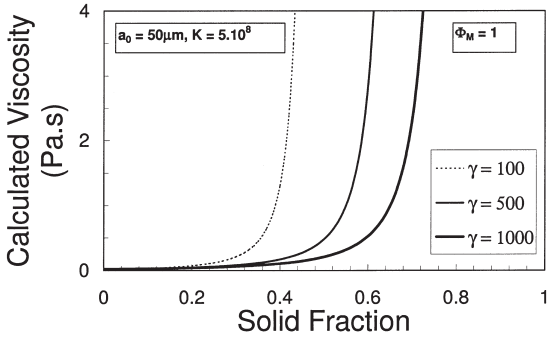


Fig. 14. Viscosity as a function of the solid fraction for different shear rates. The higher the shear rate, the higher the solid fraction leading to gelation.

its the typical profile of a semi-solid mixture [2]. The viscosity increases with the solid fraction until the solid fraction reaches a threshold value, where the suspension behaves more like a solid than a liquid. The higher the shear rate, the higher this threshold value.

## 7. COMPARISON WITH REAL MICROSTRUCTURE AND EXPERIMENTAL VISCOSITY MEASUREMENT

### *7.1. 3D microstructure visualization*

The advantage of such a simulation is the ability of viewing 3D structures. It is of interest to compare them with real structures resulting from serial cutting and micrography analysis made by Ito *et al*. [8]. Fig. 15 shows experimental and simulated 3D cluster structures. The physical parameter K [see equation (10)] has been calculated for the Al–6.5 wt% Si alloy with elementary particle radius of $a_0$=50 μm. Note that the cluster exhibited by Ito *et al*. is not representative of the population. Thus, we extracted from the simulation a cluster with comparable size.

### *7.2. Viscosity measurement*

Comparison with experimental viscosity measurement is not an easy task. Viscosity measurements are usually performed after solidification under shear rate [8]. Both the solidification and the aggregation processes take place simultaneously.

In our approach a suspension of dispersed individual globular particles is submitted to shear until it reaches its steady state of aggregation. This procedure decorrelates solidification and aggregation. However, the solidification process is assumed to have a slighter effect than the shear on both the structure and the viscosity. We then compare the simulation results with experimental viscosity measurements performed on Al–6.5 wt% Si alloys partially solidified under stirring [8]. Those experimental results were obtained with a Couette rheometer and the measurements were performed at steady state, i.e., when the shear stress is stable over time. This experimental procedure allows us to consider that the aggregation degree of the microstructure corresponds to the steady aggregation degree. The good agreement between simulation results and experimental results plotted in Fig. 16 tends to validate both the former assumption and the basis of the simulation.

### *7.3. Particle size distribution*

Fig. 17 plots the simulated distribution master curve (see Section 6) and experimental normalized size distributions resulting from microstructure analysis [19]. The master curve seems to fit the real distribution profile accurately.

## 8. CONCLUSION

The structure of semi-solid slurries results from the competition between aggregation due to surface forces and break-up induced by the shear field. The aggregation probability is set to be constant. The break-up probability is then set to be proportional to the ratio of the available kinetic energy over the rupture energy. Using a one-cluster algorithm, we supposed that the time evolution of a single cluster

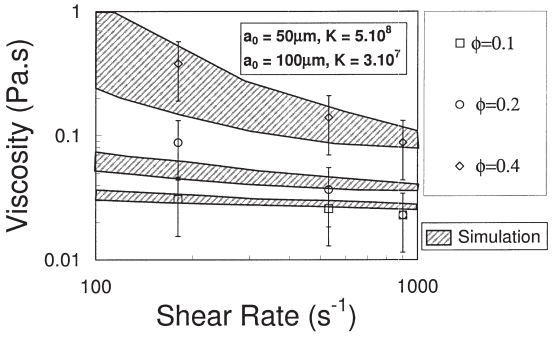


Fig. 16. Comparison between simulation results and experimental viscosity measurement of an Al–6.5 wt% Si alloy [8] as a function of the shear rate and solid fraction. Simulation results are spread over a domain limited by two reasonable values of $a_0$. This domain contains the experimental steady-state measurements.

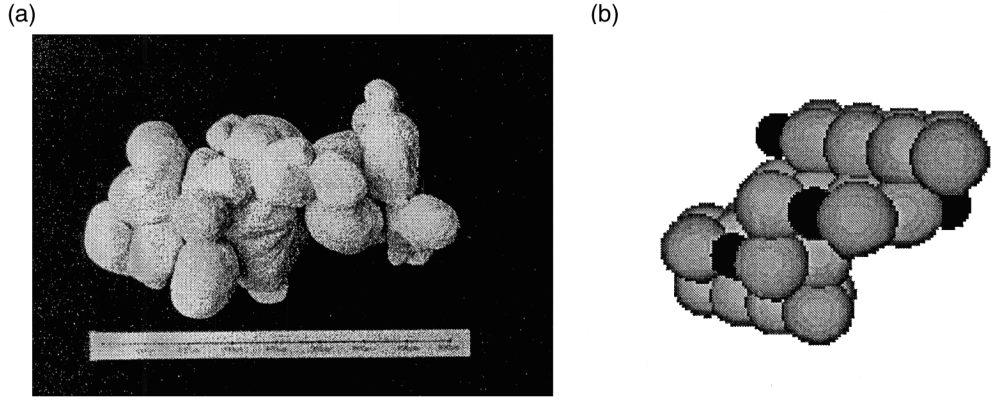


Fig. 15. Experimental and simulated cluster structure taken from an Al–6.5 wt% Si semi-solid slurry sheared at 900 $s^{-1}$. (a) 3D reconstruction extracted from Ref. [8]; (b) simulated with $K=5\times10^8$.

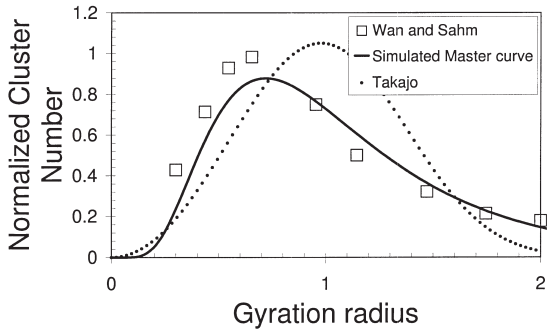


Fig. 17. Normalized cluster size distribution: comparison between experimental microstructure analysis of Wan and Sahm [19] and the present simulation. Results of Takajo *et al.* [24] are plotted for comparison. The simulated distribution seems to fit the real distribution profile accurately.

approximates the ensemble distribution of a population of clusters ("ergodic" hypothesis). Simulation of the time evolution of our representative cluster describes accurately the structure of the slurry with no adjustable parameter and estimates successfully the viscosity as a function of the applied shear rate and the volumic solid fraction. The present work allows a better understanding of the structure evolution of sheared, semi-solid metallic alloys in the $(\Phi,\dot{\gamma})$ plane. In future work, ripening could be also taken into account through a reinforcement of the necks along time after the particles encounter.

The present approach could be easily transferable to any type of suspension, in as far as the interacting forces between solid particles can be estimated.

The evaluation of the entrapped liquid fraction could be performed using a general dimension code for computing convex hulls. "QuickHulls" from the Geometry Center, University of Minnesota, USA, could provide us with a powerful tool.

*Acknowledgements*—We are grateful to C. Martin, M. Papoular, M. Suéry and A. Zavaliangos for useful discussions. This work was partly funded by Electricité De France (EDF) and CEA. One of us (M.P.) is supported by a MENRT grant and partial financial support from Région Rhône-Alpes is gratefully acknowledged.

## REFERENCES

1. Flemings, M. C., *Met. Trans. B*, 1991, **22B**, 269.
2. Joly, P. A. and Mehrabian, R., *J. Mater. Sci.*, 1976, **11**, 1393.
3. Quemada, D., *J. Méc. Th. Appl.*, 1985, 267.
4. Quemada, D., *Eur. Phys. J.*, 1998, **AP1**, 119.
5. Barnes, H. A., *J. Rheol.*, 1989, **33**, 329.
6. Krieger, I. M. and Dougherty, T. J., *Trans. Soc. Rheol.*, 1959, **3**, 137.
7. Jeffrey, D. J. and Acrivos, A., *AIChE J.*, 1976, **22**, 417.
8. Ito, Y., Flemings, C. and Cormie, J. A., in *Nature and Properties of Semi-Solids Materials*, eds J. A. Sekhar and J. A. Dantziz. TMSSan Diego, CA, 1992.
9. Poulain, P., Bibette, J. and Weitz, D. A., *Eur. Phys. J. B*, 1999, **7**, 277.
10. Buffière, J. Y., Maire, E., Lormand, P. C. G. and Fougères, R., *Acta mater.*, 1999, **47**, 1613.
11. Barbé, J. C., Perez, M. and Papoular, M., *J. Phys.: Cond. Matter*, 2000, **12**, 2567.
12. Rastogi, S. R., Wagner, N. J. and Lustig, S. R., *J. Chem. Phys.*, 1996, **104**, 9234.
13. Bradi, J. F. and Bossis, G., *Annu. Rev. Fluid Mech.*, 1988, **20**, 111.
14. Toorman, E., *Rheol. Acta*, 1997, **36**, 56.
15. Martin, C., Kumar, P. and Brown, S., *Acta metall.*, 1994, **42**, 3603.
16. Rutgers, I. R., *Rheol. Acta*, 1962, **2**, 305.
17. Laxmanan, V. and Flemings, C., *Met. Trans. A*, 1980, **11A**, 1927.
18. Wildemuth, C. R. and Williams, M. C., *Rheol. Acta*, 1984, **23**, 627.
19. Wan, G. and Sahm, P. R., *Acta metall.*, 1990, **38**, 967.
20. Mason, S. G. and Bartok, W., in *Rheology of Disperse Systems*, ed. C. Mill. Pergamon Press, Oxford, 1957.
21. Adler, P., Nadim, A. and Brenner, H., *Advances in Chemical Engineering*, vol. 15, ed. J. Wei. Academic Press, New York, 1994.
22. Ashby, M. F. and Jones, D. R. H., *Engineering Materials 1: An Introduction to Their Properties and Applications*, Paperback, Butterworth-Heinemann, MA, USA, 1996.
23. Reed, J. S., *Principles of Ceramic Processes*, 1988, Wiley-Interscience, New York, 1988.
24. Takajo, S., Kaysser, W. and Petzow, G., *Acta metall.*, 1984, **32**, 107.